frontiers in Earth Science

ORIGINAL RESEARCH
published: 24 March 2021
doi: 10.3389/feart.2021.653395

Structural Features and Evolution of the Northwestern Sichuan Basin: Insights From Discrete Numerical Simulations

Wenqiao Xu[1], Hongwei Yin[1], Dong Jia[1], Changsheng Li[2], Wei Wang[1], Gengxiong Yang[1], Wanhui He[1], Zhuxin Chen[3] and Rong Ren[3]*

[1] School of Earth Science and Engineering, Nanjing University, Nanjing, China, [2] School of Earth Science, East China University of Technology, Nanchang, China, [3] Research Institute of Petroleum Exploration and Development, Beijing, China

The northwestern Sichuan Basin has experienced Meso-Cenozoic intracontinental compressional tectonic processes and formed multi-detachment stratigraphic distribution of foreland basins and fold-thrust belts, which have caused complicated structural deformations in the deep buried layers. Rapid uplift with accelerated erosion and two sets of detachments in the Lower Triassic and Lower Cambrian controlled the multilevel deformation structure. We conducted discrete numerical simulations with double weak detachments and erosion under extrusion conditions in order to examine the mechanics and kinematics of the frontalpiedmont zones of the NW Sichuan Basin. The following findings were made. (1) With continuous compression, the weak detachments promoted the decoupled and ladder-like deformation of the thrust belt, where the deformation above the slip layer extended further than it did below it. Rapid uplift and erosion at the thrust front contributed to the formation of a passive roof fault and a monocline in the upper layer, a series of forward and backward thin-skinned thrust-buried structures in the middle layer sandwiched between two weak detachments and stacking structures in the lower layer. (2) Erosion effectively prevents the deformation from propagating above the upper detachment, but can advance a horizontal transition in the deformation style generated within the middle brittle layer: from oblique and tight fault propagation folds to symmetrical, wide, and gentle detachment folds. (3) The model results consistent with tectonic deformation in the NW Sichuan Basin indicate a possible evolutionary mechanism under compression. There is hierarchical deformation of uncoordinated contraction controlled by the Lower Triassic and Early Cambrian weak layers, with the characteristics of the shallow monocline, the middle thin-skinned thrusts, and the deeper basement-involved folds. Continuous compression contributed a sequential pattern of steps as a whole, from the frontalpiedmont zones to the foreland basin, autochthonous stacking thrusts, and the huge buried structure in the NW Sichuan Basin. During the Himalayan period, syntectonic erosion along with the uplifted thrust front maintained the development of a passive-roof duplex and a huge forward buried structure.

Keywords: Northwestern Sichuan Basin, fold-thrust belt, multiple detachments, erosion, buried structure, discrete element method

OPEN ACCESS

Edited by:
Alessandro Tibaldi,
University of Milano-Bicocca, Italy

Reviewed by:
Dan-Ping Yan,
China University of Geosciences, China
Gang Rao,
Zhejiang University, China

****Correspondence:***
Hongwei Yin
hwyin@nju.edu.cn

Specialty section:
This article was submitted to Structural Geology and Tectonics, a section of the journal Frontiers in Earth Science

Received: *14 January 2021*
Accepted: *01 March 2021*
Published: *24 March 2021*

Citation:
Xu W, Yin H, Jia D, Li C, Wang W, Yang G, He W, Chen Z and Ren R (2021) Structural Features and Evolution of the Northwestern Sichuan Basin: Insights From Discrete Numerical Simulations. Front. Earth Sci. 9:653395. doi: 10.3389/feart.2021.653395

INTRODUCTION

The northwestern Sichuan Basin, located on the eastern margin of the Tibetan Plateau and the southern front of the Qinling Orogenic Belt (**Figure 1a**), as a prospective retrogressive foreland basin since the Late Triassic, has been an important location of abundant natural gas resources and a target for development of its vast petroleum resources (Jia et al., 2006; Gorum et al., 2011; Zhao et al., 2012; Chen et al., 2019, 2020). The amalgamation of the Qiangtang Block with the North China-Kunlun-Qaidam Block and the South China Block during the Late Triassic Indosinian Orogeny and the Cenozoic India–Tibet collision (Yin and Nie, 1993; Burchfiel et al., 1995; Meng et al., 2005; Richardson et al., 2008; Royden et al., 2008; Hall, 2012; Zhang et al., 2015; Wang et al., 2016; Yan et al., 2018) accommodated a strong fold-thrust structure and crustal shortening in the Upper Yangtze area. In particular, the thrusting and uplifting of the eastern margin at the Tibetan Plateau in the Late Cenozoic and the multi-detachment stratigraphic distribution of foreland basins and fold-thrust belts ultimately led to the formation of the distinct structural features of the NW Sichuan Basin.

The front belt of the NW Sichuan region exhibits a shallow passive-roof duplex and deep-buried imbricated thrust structures (Jia et al., 2006; Jin et al., 2010; Chen et al., 2019; Fan et al., 2020), which shed some light on the structural features of intracontinental orogenic propagation in the India–Eurasian collision event. The mechanical conditions under multiple detachments (Hubbard et al., 2010; Li et al., 2019; Cui et al., 2020; Wang et al., 2020) or widespread erosion (Meng et al., 2005; Richardson et al., 2008; Yang et al., 2013; Ma et al., 2019; Fan et al., 2020) may be the reason for the adjustments in the regional tectonic stress field for the back thrust. However, due to the limitations imposed by hydrocarbon exploration in the NW Sichuan Basin and poor data quality for the area, we still need to conduct sufficient and systematic analyses of the features and evolution of the deeply buried geological structures. Numerous studies have focused on the impact of erosion or detachments on the structural evolution of fold-and-thrust belts (Couzens-Schultz et al., 2003; Konstantinovskaia and Malavieille, 2005; Bonnet et al., 2007; Hubbard and Shaw, 2009; Hao et al., 2013; Wang et al., 2013). The proposed model, without involving detachment, exhibited a uniformly spaced forward-breaking sequence with synchronous thrust activity (Morgan, 2015). The proposed model involving a detachment was almost the same as a forward in-sequence style, except that the deformation above the slip layer extended further (Cui et al., 2020). Syncontractional erosion inhibited forward propagation of the deformation front, lessening the number of major thrusts and increasing thrust activities in the hinterland (Wu and McClay, 2011). However, few studies have looked at the deformation of deep-buried thin-skinned thrust structures with two detachments under conditions of erosion.

Hence, this paper applies particle-based discrete numerical methods to simulate the development of a contractional foreland basin under multiple detachments and erosion conditions, with a particular emphasis on deep structural deformation, in order to understand the geometric characteristics of and tectonic evolution in the NW Sichuan Basin, aiming to provide principal structural understanding for regional geological studies and deep gas exploration.

TECTONIC SETTING

The architecture and evolution of the NW Sichuan Basin are largely affected by peripheral thrust belts (Burchfiel et al., 1995; Jia et al., 2006; Hubbard and Shaw, 2009; Luo et al., 2009; Wang and Meng, 2009; Thompson et al., 2015; Wang et al., 2016), especially in the Longmen Shan belt to the west and the Micang Shan to the north (**Figure 1b**). The basin developed mainly extensive marine transgression as a large intracratonic basin from Sinian to the Middle-Late Triassic (Burchfiel et al., 1995; Jia et al., 2006; Wang et al., 2016). Due to the closure of the Paleo-Tethys (Gorum et al., 2011), the basin transitioned to being fully terrestrial during the Late Triassic Indosinian Orogeny (Meng et al., 2005; Zhao et al., 2012). The NW Sichuan Basin is a top-to-the south thrusting foreland basin (Yan et al., 2018) formed during the Mesozoic that is superimposed on the extensional basin of the Late Paleozoic. Subsequently, the Cenozoic deformation involved in the growth of the Tibetan Plateau and the India–Asia collision (Royden et al., 2008; Yin, 2010) overprinted and reactivated the NE–SW trending thrust belts, giving rise to the complex basin–mountain landforms in the NW Sichuan region. Broadly speaking, the NW Sichuan Basin experienced a stronger later compression and uplift and formed fold rows with a NE–SW strike during the Jurassic and Lower Cretaceous, indicating that the later compressive strength varied along the NW–SE strike. By observing surface structures in the intraplate thrust system, the fold and fault axis strikes are found to be located mainly in NE–SW direction and are clearly controlled by the northern Longmen Shan.

In general, the NW Sichuan Basin consists of a Neoproterozoic basement of the Yangtze Craton covered by a thin, incomplete succession of Sinian to Middle Triassic shallow-marine rocks and Upper Triassic to Cretaceous terrestrial sedimentary rocks (**Figure 2**). The Sinian to Middle Triassic rocks are composed mainly of marine deposits on the craton carbonate platform and passive continental margin, and the Upper Triassic to Lower Cretaceous rocks are composed of deposits in the non-marine foreland basin (Meng et al., 2005; Royden et al., 2008). The décollement layers are an important component of the complex tectonics of the thrust belt, a marine mud shale in the Cambrian and a set of salt gypsum layers deposited in the Lower Triassic Jialingjiang–Leikoupo Formations, serving as regional weak detachments to constrain the deformation propagation and decoupling structural layers at different depths (Lu et al., 2014). The evolution of the multiphase basin led to thick filling sequences, while these sediments were always capped by widespread erosional unconformities (Richardson et al., 2008; Yang et al., 2013). Rapid lift and erosion (Richardson et al., 2008) caused almost none of the contemporary Cenozoic deposits found in the NW Sichuan Basin. The exposure of the basin interior consists of Jurassic and Lower Cretaceous rocks in the majority.

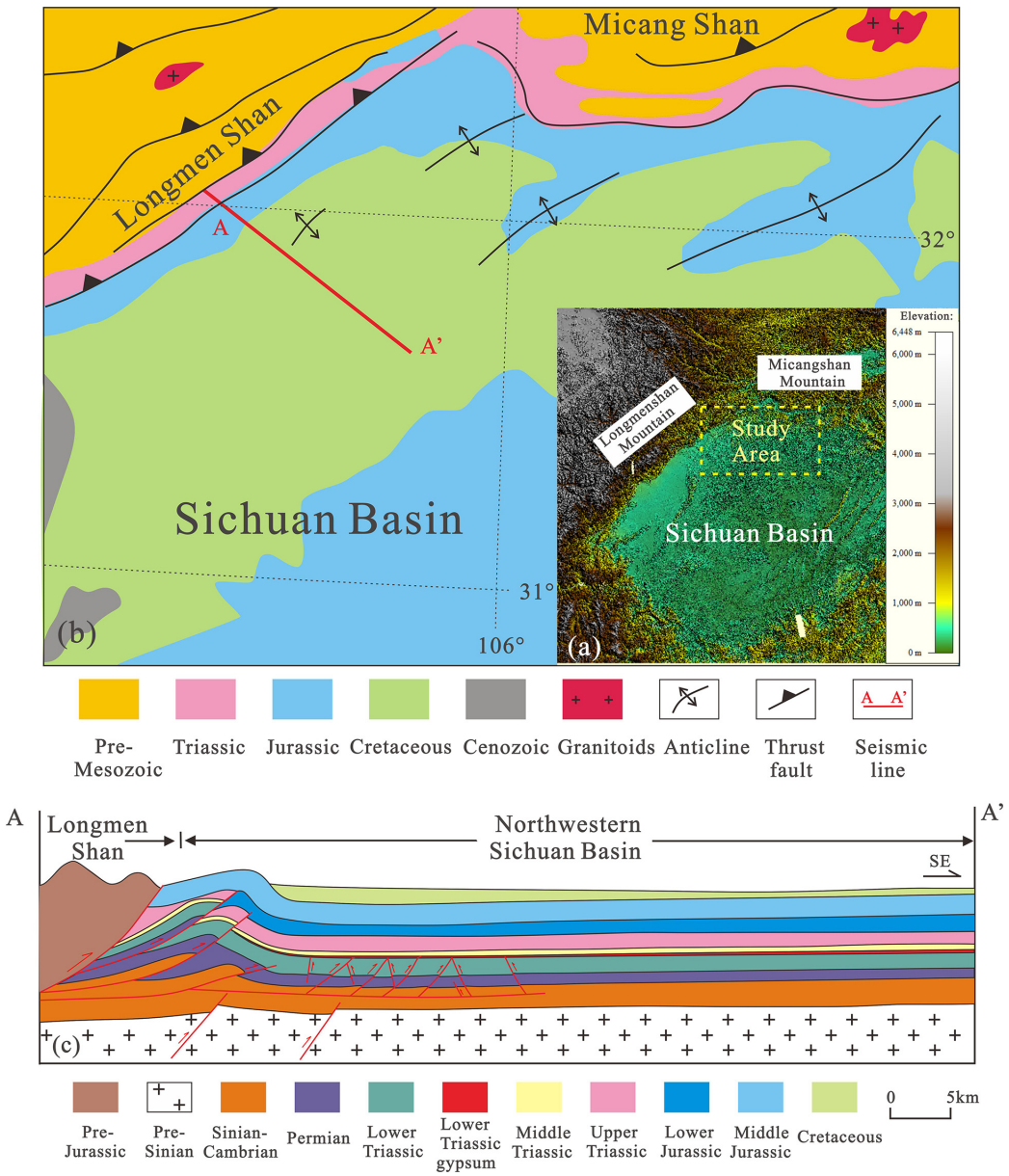

FIGURE 1 | (a) Topographic map of the Northeastern Tibetan Plateau and the NW Sichuan Basin; **(b)** enlarged simplified geological map of the study area shown in the yellow box; **(c)** AA': seismic profile of the study area. Modified after Luo et al. (2009) and Chen et al. (2019).

Based on the representative seismic profile (**Figure 1c**), the surface structure of the NW Sichuan Basin is dominated by a large anticline outcropped with the Jurassic. The Jurassic and Cretaceous rocks in a continuous sequence along the eastern side of the northern Longmen Shan belt were shallow dipping, and the folds of the different strata are generally parallel (Luo et al., 2009; Jia et al., 2010). A regional cross-section was constructed to illustrate the combination and distribution characteristics of the large-scale thrust nappes, the NW-dipping autochthonous stacking thrusts, and the huge buried structure from the orogeny to the foreland basin (Luo et al., 2009; Jin et al., 2010; Chen et al., 2019; Li et al., 2019). Seismic and well data indicate that the subsurface blind stacking thrusts are composed of three NW-dipping thrust sheets and a repetitive stratigraphic sequence. The strong stacking anticline imbricated in the front zone is in close proximity to the weak deformation in the foreland basin, including a passive duplex with shallow dipping strata and a series of buried kink structures that wedge to the southeast between the Lower Cambrian shale and the Lower Triassic evaporates. The passive roof detachment refers mainly to the back thrust and uplift of the Mesozoic strata above the salt layer of the Jialingjiang Formation. The partial kink block contains secondary thrust faults. Numerous studies have inferred that the buried deformational event in the NW Sichuan Basin

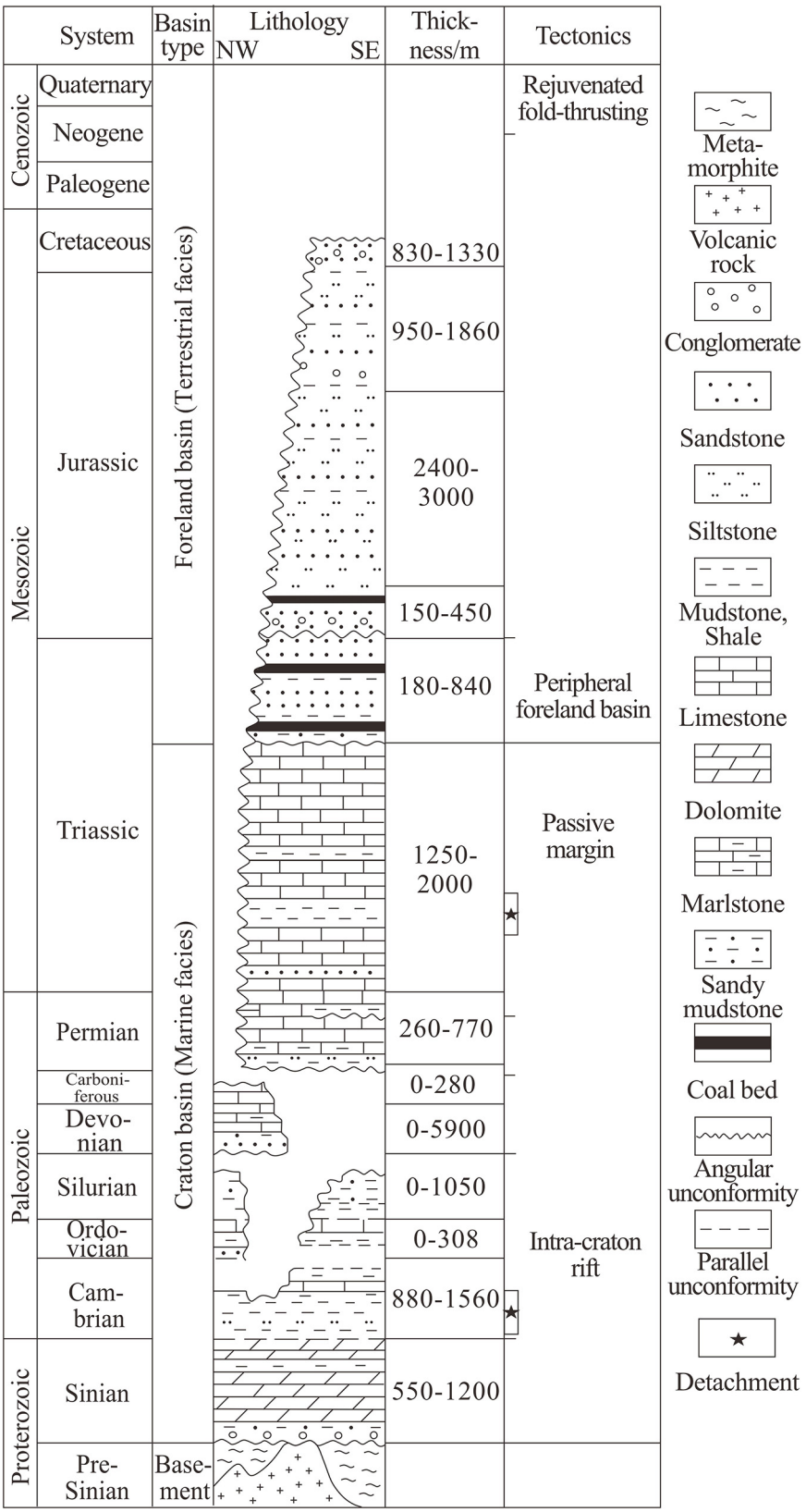

FIGURE 2 | Simplified stratigraphic column of the NW Sichuan Basin, showing multistage tectonic activities. Modified from Chen et al. (2019).

is Late Cenozoic in age and perhaps continues to the present (Luo et al., 2009; Jia et al., 2010; Chen et al., 2019). This study simulates mainly the Cenozoic deformation without considering syn-sedimentation.

METHODS AND MODEL SETUP

Discrete Element Method

The discrete element method (DEM) is a particle-based numerical approach that employs iterative calculation of particle displacement and force to solve motion via Newtonian mechanics (Cundall and Strack, 1979). Geologists have applied DEM mainly to gain insight into continuum fracture problems. Large-scale fold and thrust belt deformation, and shallow crustal rocks subject to Coulomb behavior (Burbidge and Braun, 2002; Naylor, 2005; Hardy et al., 2009; Miyakawa et al., 2010; Dean et al., 2013; Morgan, 2015; Morgan and Bangs, 2017; Liu and Konietzky, 2018; Vora and Morgan, 2019; Wang and Morgan, 2019). One of the attractions of DEM is that discrete particles under the contact mechanism can localize strain and yield emergent behavior in the system. We can use different material properties to simulate discontinuities and heterogeneities and apply the stress field of extrusion or tension. The technique resembles a numerical sandbox, but can offer added information by monitoring mechanical states correlated with deformation behavior and structure throughout the simulation and directly output the stress–strain characteristics of the deformation process.

Our implementation of DEM adopted the Hertz–Mindlin contact mechanics model (Li, 2019; Morgan, 2015). The numerical model in DEM can be denuded arbitrarily and be set different particle properties, which is suitable for studying the evolutionary process of double detachment layers in a denudation environment. Based on repeatable numerical experimental results, we studied the geometric characteristics and tectonic evolution of the NW Sichuan Basin.

Model Setup

Our two-dimensional (2-D) experimental setup (**Figure 3**) follows that of Morgan (2015), but with two detachments embedded within the sediment strata to simulate the two-detachment system of the NW Sichuan Basin. The initial model, with a size of 60 × 5.5 km, was divided into three brittle layers by two weak detachments. Particles of different colors with the same mechanical properties as the brittle layers were used as marker horizons in order to clearly observe the deformation features. The mechanical properties of the simulated system were controlled by the assigned particle properties and interparticle cohesion (**Table 1**), of which adhesion exists in the brittle layers but not in the décollements. From bottom to top: the 1.4 km-thick brittle layer denotes the Precambrian strata, the 400 m-thick lower detachment represents the Cambrian detachment, the 1.2 km-thick brittle layer represents the strata from the Cambrian to the Triassic, the 400 m-thick upper detachment depicts the Triassic Jialingjiang–Leikoupou formations, and the 2.1 km-thick upper layer serves as the cover sequence. The Cambrian detachment is composed mainly of marine mud shales and siltstone, and the Triassic detachment consists chiefly of a set of salt gypsum layers and mud shales belonging to shallow lagoon facies carbonate rocks. The lithology is not distinguished in detail in the simulation. It is divided mainly into décollement layers and brittle layers by referring to the differences in the rheological characteristics of the rocks.

Because of wide scale erosion in the study area, we designed two models with the same initial model setup but with different erosion characteristics during compression to simulate the effects of detachments and erosion on the deformation pattern of the models. Based on the low-temperature thermochronological study and erosion thermal model of a fold-thrust belt and foreland basin in the Longmen Shan region (Kirby et al., 2002; Li et al., 2012), the speeds of denudation decreased initially and increased afterward, especially during the Late Triassic and Late Cenozoic, which may be the two periods showing strong uplift in the Longmen Shan area. Model 2, in comparison, underwent accelerated erosion at shortenings of 3, 7, 10, and 12 km, indicating the shorter denudation intervals with rapid uplift representing faster rates of denudation. During each denudation process, the 1 km thickness was denuded from the top, except for the first denudation of 200 m. Model 1, as an identical simulation without erosion, defined a reference configuration. Deformation was induced by displacing the left wall at a constant velocity of 2 m/s of the domain among two low-friction décollements, modeling the compressive strength varying along the NW–SE strike during the Himalayan period.

EXPERIMENTAL RESULTS AND DISCUSSION

Model 1—No Erosion

Figures 4, **5** show the structural deformation results obtained from Model 1. We analyzed the progressive evolution of Model 1 in four stages up to a maximum shortening of 12 km and a shortening rate of 20%.

Stage 1 (shortening of 3 km and shortening rate of 5%): A fore-thrust (T1) and a back-thrust (B1) formed, resulting in a broad and gentle fold structure next to the left-moving wall (**Figure 4B**). In the upper layer, the strain was distributed widely along Décollement 1 and formed a gentle passive roof at the front limb. T1 slipped forward and developed two ramp-flat faults in the multilevel detachments, where the extent of the upper ramp-flat fault was much wider than that of the lower one (**Figure 5A**). The maximum shear stress increased in zones adjacent to the moving wall and the monocline of the brittle cover (**Figure 5E**). The highest values of maximum shear stress occurred on the front of the frontal thrusts, outlining regions of unfaulted material.

Stage 2 (shortening of 7 km and shortening rate of 11.7%): The structural layers in depths divided by weak detachments were decoupled, where the newly formed thin-skinned thrusts between detachments did not synchronize with the upper brittle strata. The extension of T1 broke through the upper layer and developed a pop-up structure (**Figure 4C**), while a series of gentle kink folds were formed and sandwiched successively between the detachments associated with new thrusts T2, B2, T3, and B3

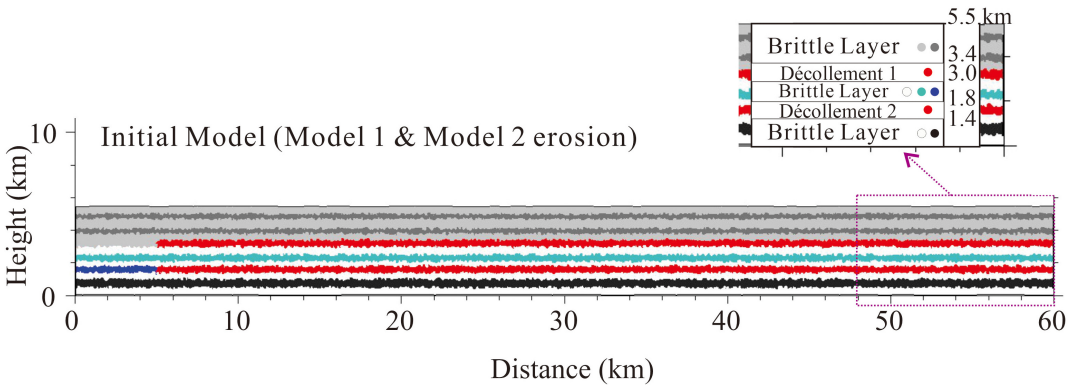

FIGURE 3 | Initial model setup.

TABLE 1 | Parameter setting for the DEM model.

Unit	Radii (m)	Shear modulus (Pa)	Poisson's ratio	Friction coefficient	Density (kg/m^3)	Young's modulus (Pa)	Color
Upper layer	60, 80	2.90×10^9	0.2	0.3	2500	2.0×10^8	
Décollement 1	60, 80	2.90×10^9	0.2	0.0	2200	2.0×10^8	
Middle layer	60, 80	2.90×10^9	0.2	0.3	2500	2.0×10^8	
Décollement 2	60, 80	2.90×10^9	0.2	0.0	2200	2.0×10^8	
Lower layer	60, 80	2.90×10^9	0.2	0.3	2500	2.0×10^8	

(**Figure 5B**). Red detachment particles were accumulated at the crests and troughs of the kink belts. Continuous compression caused the dominant deformation to be controlled by the faults of T1 and B1, with a significant increase in displacement. In addition, ramp-flat faults slid wider along the detachments, especially the upper one. The maximum shear stress was distributed step by step (**Figure 5F**), where the upper layer spread farthest, the middle layer accumulated near the folds, and the lower layer was transported a limited distance, but stronger than the others.

Stage 3 (shortening of 10 km and shortening rate of 16.7%): T2 shared a similar trace to T1 through cutting the upper layer upward and causing the maximum shear stress to be transported forward to the new unfaulted front limb (**Figure 4D**). Meanwhile, kink belts propagated forward, where the deformation style of the original gentle folds changed to being tight and oblique. The new-born folds generated within the middle brittle layer remained symmetrical, wide, and gentle. With the rupture of T3 and B3 (**Figure 5C**), the range of stress accumulation in the middle layer became smaller (**Figure 5G**). Deformation beneath the Décollement 2 began to form stacking imbricating structures, but were still limited in the hinterland.

Stage 4 (shortening of 12 km and shortening rate of 20%):The various brittle layers displayed different progressive deformations to transform the strain forward (**Figure 4E**). The latest principal strain within the thrust belt presented as the jumping forward of the thrust front. When a frontal pop-up structure was shaped by B6, T7, and B7 (**Figure 5D**), the stress decreased sharply on the left of B6 but was transferred forward along the upper detachment (**Figure 5H**). The formation of B6 through the upper layer caused a stress weak zone above the upper detachment, which led to stress between detachments being transferred forward and gathered beneath B6. Therefore, there was a horizontal transitional deformation in the middle layer generated from the backstop to the area below B6: from oblique and tight fault-propagation folds in the hinterland to relatively symmetrical, wide, and gentle detachment folds in the foreland, from steeper and large-inclination-angle Y-shaped fault groups (T3 and B3, T4, and B4) to gentle hedge structures (T5 and B5, B8). Deformation beneath Décollement 2 formed stacking structures via three imbricate faults, but was still limited to the hinterland.

Model 2—Accelerated Erosion

The evolution of Model 2 with a total shortening of 12 km and a shortening rate of 20% (**Figure 6**) can be divided into four deformation stages accompanied by four times of denudation. With the increase in shortening and the height of the hinterland, the erosions were added to the model and the interval of denudation became shorter where the strata were denuded to a height of 6 km at a shortening rate of 5%, a height of 7 km at a shortening rate of 11.7%, and a height of 8 km at shortening rates of 16.7 and 20%. During each denudation process, the 1 km thickness was denuded from the top, except for the first denudation of 200 m. The uneven surface following denudation was due to the spring-back of elastic particles.

The first deformation stage (shortening of 3 km and shortening rate of 5%) was almost the same as those of Model 1 except for being denuded to 6 km: one fore-thrust (T1) formed toward the foreland and one back-thrust (B1) formed the first stage (**Figure 6B**). Similarly, T1 still slipped forward and developed two ramp-flat faults in two detachments,

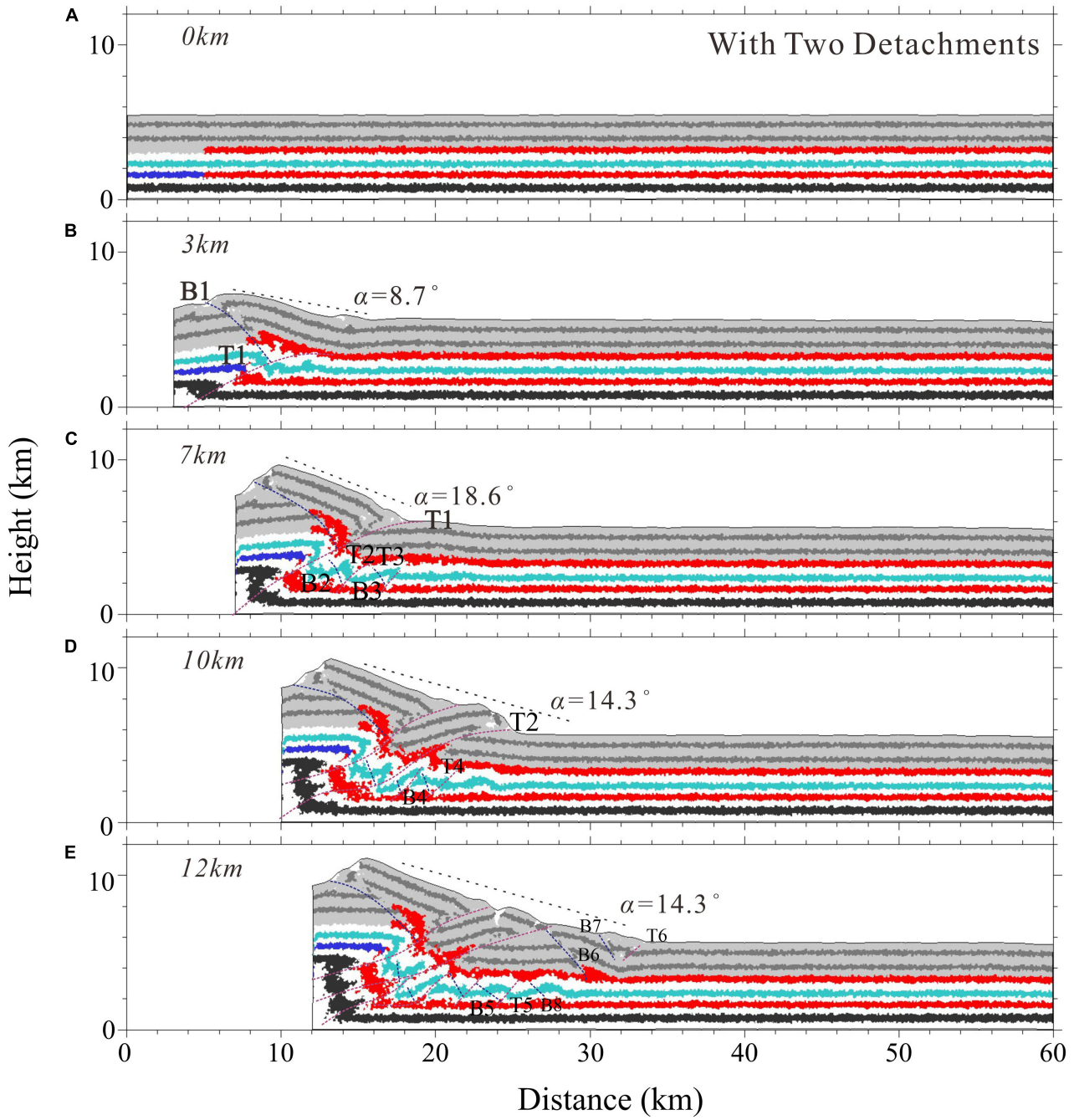

FIGURE 4 | Modeled progress with two detachments due to the left-wall displacement at shortening distances of **(A)** 0 km, **(B)** 3 km, **(C)** 7 km, **(D)** 10 km, and **(E)** 12 km. T1–T6 and B1–B8 denote fore-thrusts and back-thrusts, respectively, in the order of their formation;αrepresents the current slope angle.

where the upper flat-ramp fault extended much wider than the lower one (**Figure 7A**). The erosion meant that the wedge taper angle became gentle, but the monocline above the back-thrust changed from a gentle tilt to a steeper one. The most significant difference was in the maximum shear stress. The reduction in load as a result of denudation released the originally accumulated stress near the monoclinal inflection point and the extrusion backstop. The stress was concentrated mainly at the lower layer in the hinterland due to its depth and compression (**Figure 7E**).

Stage 2 represents a model being denuded to 7 km at a shortening rate of 11.7%. The structural style of the thrust belt was formed into a passive-roof duplex back-thrust (B1) along the upper detachment (**Figure 6C**). In the upper brittle layer, shortening was absorbed by the slip of the back-thrust along the upper detachment. Meanwhile, T4 was formed due to

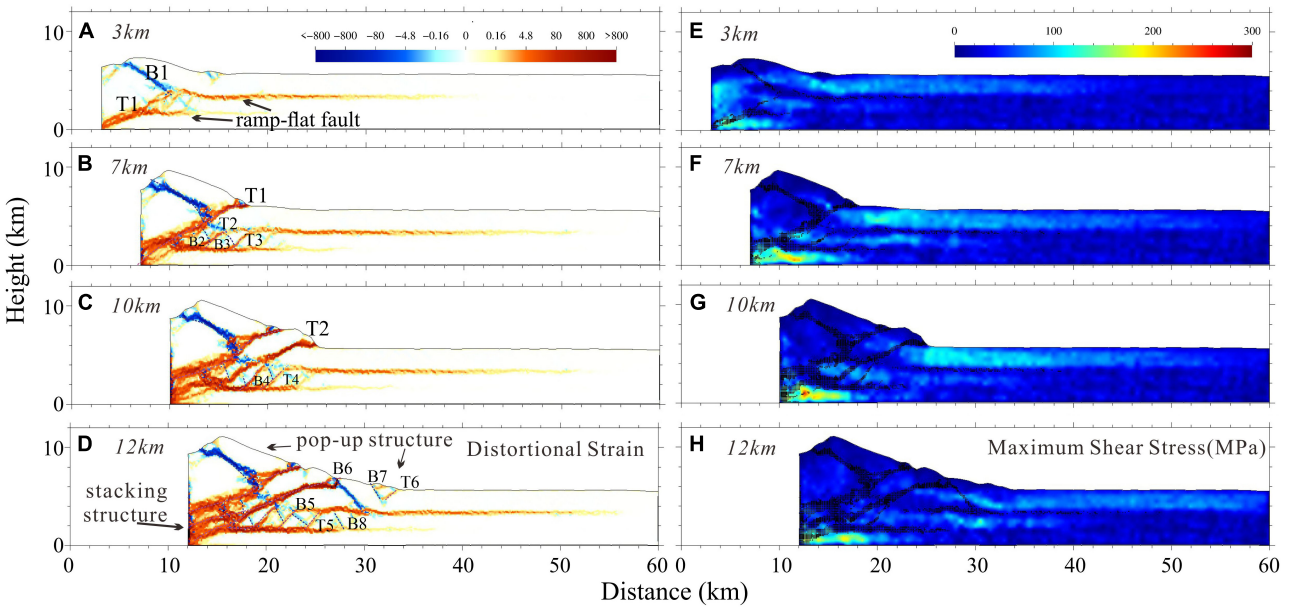

FIGURE 5 | Final distortional strain field (left) and final maximum shear stress field (right) for simulation with two detachments at shortening distances of **(A,E)** 3 km, **(B,F)** 7 km, **(C,G)** 10 km, and **(D,H)** 12 km. Shear strain magnitude is shown by color intensity. Red indicates top-to-the-right sense of shear; blue indicates top-to-the-left sense of shear. Stress intensity scales with color. T1–T6 and B1–B8 denote fore-thrusts and back-thrusts, respectively, in the order of their formation.

stress accumulated strongly enough at the monoclinal inflection point that T1 cut through (**Figure 7B**).However, under the influence of denudation, there was a mistake between T1 and T4. In the middle, decoupling deformation resulted in two fault-propagation folds and led to T2, B2, T3, and B3 being asymmetrically formed sequentially. The stress was still ladder-like, but it was weaker than that before denudation (**Figure 7F**).

Stage 3 corresponds to a model shortening rate from 11.7 to 16.7% and being denuded to 8 km. In the upper brittle layer, the structural deformation was still dominated by the passive duplex roof along the upper décollement level instead of the leaping structures. The monocline layer shifted more steeply, and the wedge front propagated farther without obvious displacement inside (**Figure 6D**). With shortening increasing, the fault-related folds passed forward and B4 and T5 were formed in the middle layer, giving rise to a certain lift in the foreland (**Figure 7C**). Because of the strong basal friction, sequential thrust faults developed along the basal detachment, forming a stacking structure at the bottom that raised the height of the hinterland. On the maximum shear stress map (**Figure 7G**), it is difficult for stress to be concentrated in the cover under erosion, thus preserving the integrity of the passive roof. The inflection point of the monocline was still the best breakthrough point of the faults, and a slight deformation can be seen in the strain diagram.

During Stage 4, the model was shortened from 16.7 to 20% and denuded to 8 km. The evolutionary progress was similar to Stage 3 (**Figure 6E**). The shortening of the model resulted in the monocline being uplifted by the bottom stacking structure. The forward transfer of the faults (B5, T6) reduced the degree of the slope angles slightly (**Figure 7D**). Under the dual influence of extrusion and denudation, the transition from the asymmetric and tight folds at the back edge to the symmetrical and loose folds at the front thrusts was complete, and the maximum shear stress spread farther (**Figure 7H**).

DISCUSSION

Effect of Erosion on the Thrust Wedge Tapers With Two Detachments

Denudation causes a reduction in the overlying load. Due to this reduction, the amount of overlap between particles (δ_n) is reduced, and then elastic particles will rebound within a certain range. At the same time, the localized deformation fracture follows a law similar to Coulomb's fracture criterion for the shear force (f_s) and repulsive normal forces (f_n):

$$f_s \leq \mu f_n + C;\ f_n = k_n \delta_n$$

where k_n represents the normal interparticle stiffness, μ represents the friction on the particle surfaces, and C is the cohesion strength. When maximum shear force is reached at a fixed shear strength, slip occurs, allowing particles to slide past each other. By this mechanism, faults can develop and grow. Thus, the erosion imposed on the model lowers the normal stress and subsequently also lowers the shear strength. With the increase in erosion and the decrease in load, the particles in the brittle layer along the upper detachment rebound, so that the maximum shear stress cannot be concentrated at the inflection point of the monocline and be large enough to form a new fault, but is more dispersed in the foreland leading edge. Although the shear strength is reduced, however, there is no direct erosion in the middle brittle layer, the stress does not dissipate significantly, with sufficient shear stress meeting the decreased shear strength

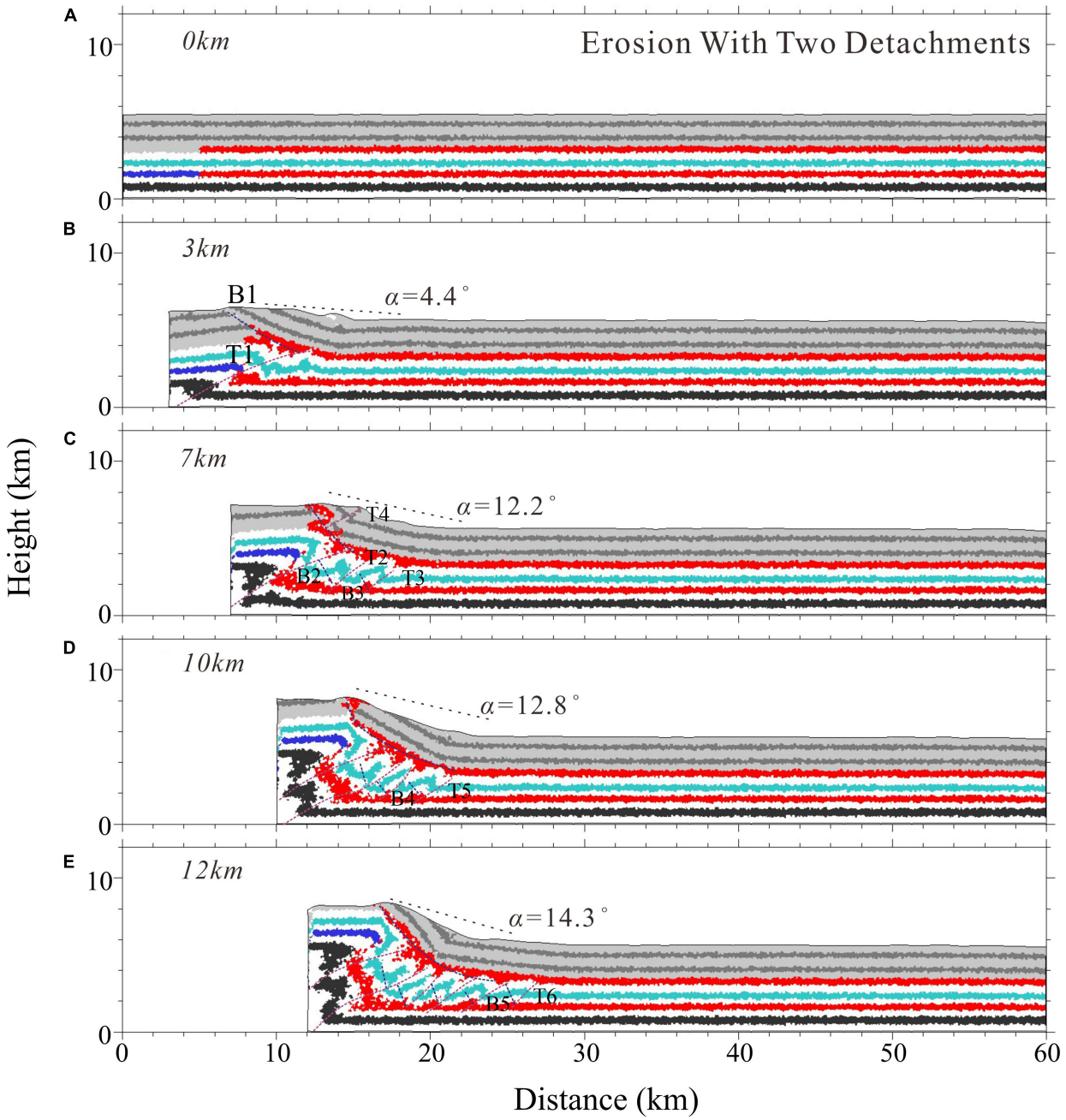

FIGURE 6 | Modeled progress with two detachments and erosions due to the left-wall displacement at shortenings of **(A)** 0 km, **(B)** 3 km, **(C)** 7 km, **(D)** 10 km, and **(E)** 12 km. T1–T6 and B1–B5 denote fore-thrusts and back-thrusts, respectively, in the order of their formation;αrepresents the current slope angle.

and then forming a group of forward transitive fault propagation folds. The double weak detachment layers experience an obvious decoupling deformation, and the distribution of maximum shear stress will be stepped, where the shallower the layer, the farther it spreads. The upper detachment layer has high mobility, while the middle detachment layer is controlled by the formation range of the folds.

Critical tapered-wedge theory was first proposed in the 1980s (Davis et al., 1983; Dahlen, 1984, 2003) and has been successfully applied to the study of the deformation mechanism and kinematic evolution of fold-and-thrust belts and accretionary prisms in compressional settings (Dahlen, 2003; Morley, 2007; Dedontney and Hubbard, 2012; Wang et al., 2013; Sun et al., 2016). The theory indicates that the critically tapered wedge, as a stable geometry, slides along the basal décollement without internal deformation and is dependent on the basal friction coefficient and the internal strength of the material. Therefore, when the wedges are in subcritical or supercritical states,

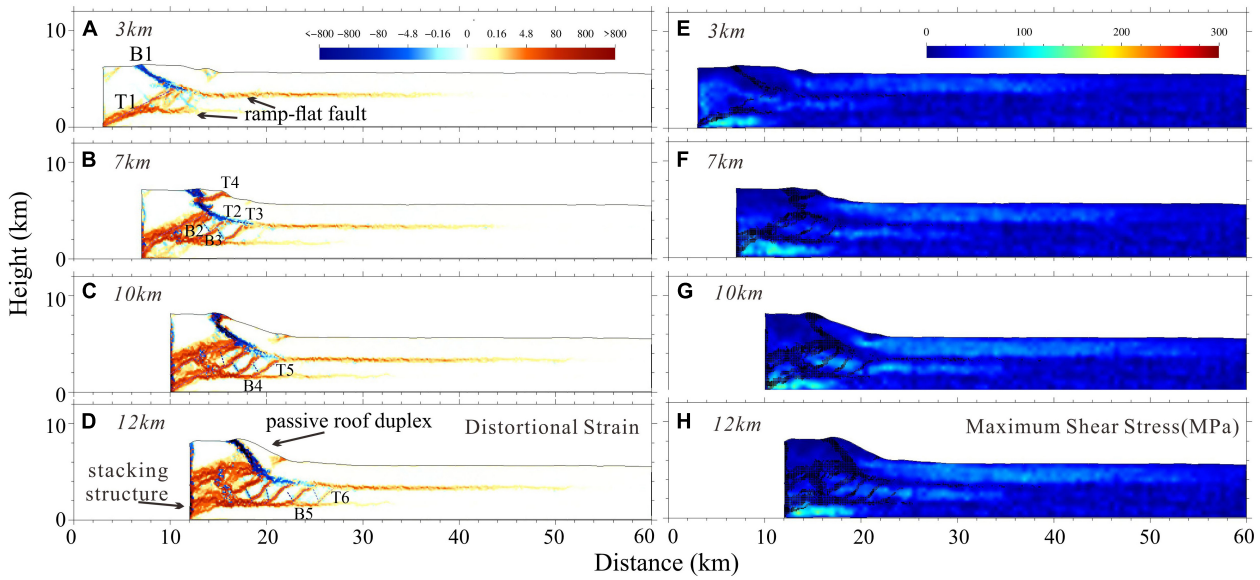

FIGURE 7 | Final distortional strain field (left) and final maximum shear stress field (right) for the simulation with two detachments and erosions at shortenings of **(A,E)** 3 km, **(B,F)** 7 km, **(C,G)** 10 km, and **(D,H)** 12 km. The shear strain magnitude is shown by color intensity; red indicates the top-to-the-right sense of shear; blue indicates the top-to-the-left sense of shear. Stress intensity scales with color. T1–T6 and B1–B5 denote fore-thrusts and back-thrusts, respectively, in the order of their formation.

adjustments are required for internal unstable structures to gain critical taper. The subcritical wedge will internally form new thrusts or reactivate old thrusts to increase the slope angle, while the supercritical wedge may propagate deformation by jumping in the front limb to decrease its taper.

In Model 1 without denudation, as the thrust zone extends forward, the thrust front leaps forward instead of mainly sliding forward to maintain a critical taper (**Figure 8**). The state of the wedge accommodates states from subcritical to supercritical, and adjustments to their geometries are required for them to gain a stable critical taper. When the wedge at the front of the thrust belt is in a subcritical state, the ramp-flat structure and vertical uplift in the hinterland increases the slope angle to approach the critical angle. As the slope angle increases beyond the critical state, the intermediate horizontal shear zone passes upward and cuts through, and then the pop-up structure along the upper detachment jumps forward sequentially to stabilize the propagation of the tectonic deformation in a critical state. In the supercritical state, the fore-thrust of T1 is primarily reactivated and cuts through, destroying the passive roof, to reduce the slope angle. The upward breakthrough of the T1 is the key to the failure to preserve the passive roof.

In Model 2, denudation reduces the taper angle in order to hold it away from the state when T1 begins to cut upward (**Figure 8**), ensuring the integrity of the passive roof. The slope angle swings back and forth between the T1 critical upward transmission and the subcritical state. When the wedge at the front of the passive roof belt is in a subcritical state, back-thrusting along the upper décollement steepens the wedge so as to approach the critical angle. The deformation styles from the subcritical to the supercritical state rely on the steepened passive roof, from tight fault propagation folds to loose detachment folds sandwiched between two detachment layers and superimposed on the stacking structure. With the erosion continuing to decrease the slope, the passive back-thrust along the upper detachment remains active and inhibits the fore-thrust developing at the thrust front, leading to the sustained passive-roof duplex. Accompanied by continuous erosion, the deformation front is controlled mainly by the buried thin thrusts and kink fold structure sandwiched between two weak detachments. There was a gradual transition in the deformation style generated within the middle brittle layer: from asymmetrical, tight, and foreland-convergent fault propagation folds in the hinterland, affected mainly by extrusion, to symmetrical, wide, and gentle décollement folds in the foreland under the combined influence of extrusion and denudation. The distance at which the buried folds pass forward depends on the extent of the middle detachment layer and the slope angle of the frontal region of the passive roof. Continuous erosion and extrusion allow buried folds to pass forward to a certain extent.

Mechanism and Evolution of the NW Sichuan Basin

Of the two numerical models, Model 2 showed the greater similarity with the natural geological model in the NW Sichuan Basin in terms of the autochthonous stacking thrusts, huge buried structures, and passive duplex roof. Geological cross-sections revealed that the passive roof layer had no obvious displacement or thrusting forward into the basin via the upper detachment, but instead consisted of a series of tight and asymmetric thin-skinned fore-thrust and back-thrust structures located between the two weak detachments, and multiple unconformable relations since the Late Triassic corresponded to denudation events occurring

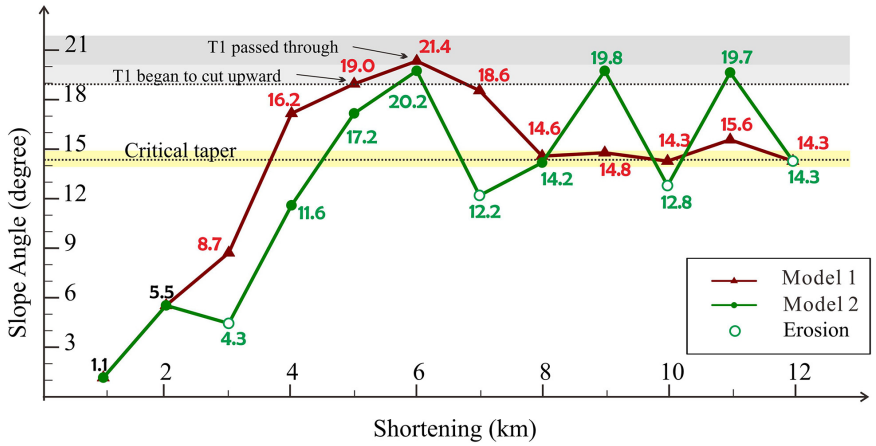

FIGURE 8 | Comparison of the slope angle versus shortening for the two models.

from the Mesozoic to the Cenozoic, especially the Cenozoic India–Asia collision that built up rapid lift and extensive denudation. This similarity suggests two pivotal factors for the deformation of the NW Sichuan foreland basin: (i) the decoupling effect of the detachments causing the Late Triassic gypsum salt bed and Early Cambrian sand shale to act as two weak detachments dominating the tectonic deformation style of the thrust belt, and (ii) the extent to which erosion plays an important role in shaping the present structural framework of the NW Sichuan Basin. We have concluded that denudation results in the spring-back of strata and the activation of the back-thrust fault along the upper detachment, so that the maximum shear stress cannot be concentrated in the upper structural layer to ensure the integrity of the passive roof. Moreover, erosion reduces the shear strength related to fault formation, engendering a series of complex buried structures in the middle structural layer. The stacking structure is formed in the lower structural layer due to strong basal friction. The maintenance of a passive-roof duplex in the NW Sichuan Basin depends mainly on continuous compression and denudation in the Himalayan period.

CONCLUSION

We have used the discrete element method (DEM) to carry out a numerical simulation of the deformation mechanism of the fold-and-thrust belt in NW Sichuan Basin, and we draw the following conclusions.

(1) With continuous compression, the weak detachments promoted the decoupled and ladder-like deformation of the thrust belt, where the deformation above the slip layer extended further than that below it. Rapid uplift and erosion at the thrust front contributed to the formation of a passive roof fault and a monocline in the upper layer, a series of forward and backward thin-skinned thrust buried structures in the middle layer sandwiched between two weak detachments, and stacking structures in the lower layer.

(2) Erosion effectively prevents the deformation from propagating above the upper detachment, but can advance a horizontal transition in the deformation style generated within the middle brittle layer: from oblique and tight fault propagation folds to symmetrical, wide, and gentle detachment folds.

(3) The model results consistent with tectonic deformation in the NW Sichuan Basin indicate a possible evolutionary mechanism under compression. There is hierarchical deformation of uncoordinated contraction controlled by the Lower Triassic and Early Cambrian weak layers showing the characteristics of a shallow monocline, the middle thin-skinned thrusts, and the deeper basement-involved folds. Continuous compression contributed overall a sequential pattern of steps from the frontalpiedmont zones to the foreland basin, autochthonous stacking thrusts, and the huge buried structure in the NW Sichuan Basin. During the Himalayan period, syntectonic erosion, along with the uplifted thrust front, maintained the development of a passive-roof duplex and a huge forward buried structure.

DATA AVAILABILITY STATEMENT

The raw data supporting the conclusions of this article will be made available by the authors, without undue reservation.

AUTHOR CONTRIBUTIONS

WX: conceptualization, methodology, software, validation, formal analysis, investigation, resources, data curation, writing—original draft, writing—review and editing, visualization, and supervision. HY: conceptualization, methodology, investigation, resources, writing—original draft, writing—review and editing, visualization, supervision, project administration, and funding

acquisition. DJ: methodology, investigation, data curation, writing—original draft, writing—review and editing, visualization, supervision, project administration, and funding acquisition. CL: methodology, software, validation, resources, and visualization. WW: software, validation, formal analysis, and writing—review and editing. GY and WH: formal analysis, validation, and writing—review and editing. ZC and RR: conceptualization, investigation, resources, project administration, and funding acquisition. All authors contributed to the article and approved the submitted version.

FUNDING

We gratefully acknowledge the financial support provided by the National Natural Science Foundation of China (41972219 and 41572187), the National S&T Major Project of China (2016ZX05003-001 and 2017ZX05008-001-001), and the CNPC Ultra-Deep Hydrocarbon Research Project (2018A-0101).

ACKNOWLEDGMENTS

We thank our editor AT and the two reviewers for their constructive comments and helpful suggestions. The numerical calculations in this manuscript were performed at the computing facilities of the High Performance Computing Center (HPCC) of Nanjing University. HY would like to thank Prof. Julia Morgan and Rice University for hosting his collaborative visit in 2009, providing him with the opportunity to further develop his knowledge of DEM and geomechanics principles and to learn the capabilities of these methods.

REFERENCES

Bonnet, C., Malavieille, J., and Mosar, J. (2007). Interactions between tectonics, erosion, and sedimentation during the recent evolution of the Alpine orogen: analogue modeling insights. *Tectonics* 26:TC6016.

Burbidge, D. R., and Braun, J. (2002). Numerical models of the evolution of accretionary wedges and fold-and-thrust belts using the distinct-element method. *Geophys. J. Int.* 148, 542–561. doi: 10.1046/j.1365-246x.2002.01579.x

Burchfiel, B. C., Zhiliang, C., Yupinc, L., and Royden, L. H. (1995). Tectonics of the Longmen Shan and adjacent regions, Central China. *Int. Geol. Rev.* 37, 661–735. doi: 10.1080/00206819509465424

Chen, Z., Li, W., Wang, L., Lei, Y., Yang, G., Zhang, B., et al. (2019). Structural geology and favorable exploration prospect belts in northwestern Sichuan Basin, SW China. *Pet. Explor. Dev.* 46, 413–425. doi: 10.1016/s1876-3804(19)60022-4

Chen, Z., Wang, L., Yang, G., Zhang, B., Ying, D., Yuan, B., et al. (2020). Geological structures and potential petroleum exploration areas in the southwestern Sichuan fold-thrust belt, SW China. *Pet. Explor. Dev.* 47, 699–713. doi: 10.1016/s1876-3804(20)60086-6

Couzens-Schultz, B. A., Vendeville, B. C., and Wiltschko, D. V. (2003). Duplex style and triangle zone formation: insights from physical modeling. *J. Struct. Geol.* 25, 1623–1644. doi: 10.1016/s0191-8141(03)00004-x

Cui, J., Jia, D., Yin, H., Chen, Z., Li, Y., Wang, M., et al. (2020). The influence of a weak upper ductile detachment on the Longmen Shan fold-and-thrust belt (eastern margin of the Tibetan Plateau): insights from sandbox experiments. *J. Asian Earth Sci.* 198:104220. doi: 10.1016/j.jseaes.2019.104220

Cundall, P. A., and Strack, O. D. L. (1979). A discrete numerical mode for granular assemblies. *Géotechnique* 29, 47–65. doi: 10.1680/geot.1979.29.1.47

Dahlen, F. A. (1984). Noncohesive critical Coulomb wedges: an exact solution. *J. Geo. Res.* 89:10125. doi: 10.1029/jb089ib12p10125

Dahlen, F. A. (2003). Critical taper model of fold-and-thrust belts and accretionary wedges. *Ann. Rev. Earth Planet. Sci.* 18, 55–99. doi: 10.1146/annurev.ea.18.050190.000415

Davis, D., Suppe, J., and Dahlen, F. A. (1983). Mechanics of fold-and-thrust belts and accretionary wedges. *J. Geophys. Res. Atmos.* 88, 1153–1172. doi: 10.1029/jb088ib02p01153

Dean, S. L., Morgan, J. K., and Fournier, T. (2013). Geometries of frontal fold and thrust belts: insights from discrete element simulations. *J. Struct. Geol.* 53, 43–53. doi: 10.1016/j.jsg.2013.05.008

Dedontney, N., and Hubbard, J. (2012). Applying wedge theory to dynamic rupture modeling of fault junctions. *Bull. Seismol. Soc. Am.* 102, 1693–1711. doi: 10.1785/0120110190

Fan, X., Jia, D., Yin, H., Shen, L., Liu, J., Cui, J., et al. (2020). Analogue modeling of the northern Longmen Shan thrust belt (eastern margin of the Tibetan plateau) and strain analysis based on particle image velocimetry. *J. Asian Earth Sci.* 198, 104238. doi: 10.1016/j.jseaes.2020.104238

Gorum, T., Fan, X., van Westen, C. J., Huang, R. Q., Xu, Q., Tang, C., et al. (2011). Distribution pattern of earthquake-induced landslides triggered by the 12 May 2008 Wenchuan earthquake. *Geomorphology* 133, 152–167. doi: 10.1016/j.geomorph.2010.12.030

Hall, R. (2012). Late Jurassic–Cenozoic reconstructions of the Indonesian region and the Indian Ocean. *Tectonophysics* 570-571, 1–41. doi: 10.1016/j.tecto.2012.04.021

Hao, F., Zou, H. Y., and Lu, Y. C. (2013). Mechanisms of shale gas storage: implications for shale gas exploration in China. *AAPG Bull.* 97, 1325–1346. doi: 10.1306/02141312091

Hardy, S., McClay, K., and Muñoz, J. A. (2009). Deformation and fault activity in space and time in high-resolution numerical models of doubly vergent thrust wedges. *Mar. Pet. Geol.* 26, 232–248. doi: 10.1016/j.marpetgeo.2007.12.003

Hubbard, J., and Shaw, J. H. (2009). Uplift of the Longmen Shan and Tibetan plateau, and the 2008 Wenchuan (M = 7.9) earthquake. *Nature* 458, 194–197. doi: 10.1038/nature07837

Hubbard, J., Shaw, J. H., and Klinger, Y. (2010). Structural setting of the 2008 Mw7.9 Wenchuan, China, earthquake. *Bull. Seismol. Soc. Am.* 100, 2713–2735. doi: 10.1785/0120090341

Jia, D., Li, Y., Lin, A., Wang, M., Chen, W., Wu, X., et al. (2010). Structural model of 2008 Mw 7.9 Wenchuan earthquake in the rejuvenated Longmen Shan thrust belt, China. *Tectonophysics* 491, 174–184. doi: 10.1016/j.tecto.2009.08.040

Jia, D., Wei, G., Chen, Z., Li, B., Zeng, Q., and Yang, G. (2006). Longmen Shan fold-thrust belt and its relation to the western Sichuan Basin in central China: new insights from hydrocarbon exploration. *AAPG Bull.* 90, 1425–1447. doi: 10.1306/03230605076

Jin, W., Tang, L., Yang, K., Wan, G., and Lü, Z. (2010). Segmentation of the Longmen mountains thrust belt, Western Sichuan Foreland Basin, SW China. *Tectonophysics* 485, 107–121. doi: 10.1016/j.tecto.2009.12.007

Kirby, E., Reiners, P. W., Krol, M. A., Whipple, K. X., Hodges, K. V., Farley, K. A., et al. (2002). Late Cenozoic evolution of the eastern margin of the Tibetan Plateau: inferences from40Ar/39Ar and (U-Th)/He thermochronology. *Tectonics* 21:1-1-1-20.

Konstantinovskaia, E., and Malavieille, J. (2005). Erosion and exhumation in accretionary orogens: experimental and geological approaches. *Geochem. Geophys. Geosyst.* 6:Q02006.

Li, C. (2019). *Quantitative Analysis and Simulation of Structural Deformation in the Fold and Thrust Belt Based on Discrete Element Method*. 1·289. Doctor thesis, NanJing University, NanJing. (in Chinese with English abstract).

Li, Y., Lu, R., He, D., Wang, X., Liu, Y., Xu, X., et al. (2019). Transformation of coseismic faults in the northern Longmenshan tectonic belt, eastern Tibetan Plateau: implications for potential earthquakes and seismic risks. *J. Asian Earth Sci.* 177, 66–75. doi: 10.1016/j.jseaes.2019.03.013

Li, Z. W., Liu, S., Chen, H., Deng, B., Hou, M., Wu, W., et al. (2012). Spatial variation in Meso-Cenozoic exhumation history of the Longmen Shan thrust belt (eastern Tibetan Plateau) and the adjacent western Sichuan basin:

constraints from fission track thermochronology – Sciencedirect. *J. Asian Earth Sci.* 47, 185–203. doi: 10.1016/j.jseaes.2011.10.016

Liu, Y., and Konietzky, H. (2018). Particle−based modeling of pull−apart basin development. *Tectonics* 37, 4700–4713. doi: 10.1029/2018tc004973

Lu, R., He, D., John, S., Wu, J. E., Liu, B., and Chen, Y. (2014). Structural model of the central Longmen Shan thrusts using seismic reflection profiles: implications for the sediments and deformations since the Mesozoic. *Tectonophysics* 630, 43–53. doi: 10.1016/j.tecto.2014.05.003

Luo, L., Jia, D., Li, H., Li, Y., Deng, F., Chen, Z., et al. (2009). Magnetic fabric investigation in the northwestern Sichuan Basin and its regional inference. *Phys. Earth Planet. Inter.* 173, 103–114. doi: 10.1016/j.pepi.2008.11.004

Ma, X. H., Yang, Y., Wen, L., and Luo, B. (2019). Distribution and exploration direction of medium- and large-sized marine carbonate gas fields in Sichuan Basin, SW China. *Pet. Explor. Dev.* 46, 1–15. doi: 10.1016/s1876-3804(19)30001-1

Meng, Q.-R., Wang, E., and Hu, J.-M. (2005). Mesozoic sedimentary evolution of the northwest Sichuan basin: implication for continued clockwise rotation of the South China block. *Geol. Soc. Am. Bull.* 117, 396–410. doi: 10.1130/b25407.1

Miyakawa, A., Yamada, Y., and Matsuoka, T. (2010). Effect of increased shear stress along a plate boundary fault on the formation of an out-of-sequence thrust and a break in surface slope within an accretionary wedge, based on numerical simulations. *Tectonophysics* 484, 127–138. doi: 10.1016/j.tecto.2009.08.037

Morgan, J. K. (2015). Effects of cohesion on the structural and mechanical evolution of fold and thrust belts and contractional wedges: discrete element simulations. *J. Geophys. Res. Solid Earth* 120, 3870–3896. doi: 10.1002/2014jb011455

Morgan, J. K., and Bangs, N. L. (2017). Recognizing seamount-forearc collisions at accretionary margins: insights from discrete numerical simulations. *Geology* 45, 635–638. doi: 10.1130/g38923.1

Morley, C. K. (2007). Interaction between critical wedge geometry and sediment supply in a deep-water fold belt. *Geology* 35, 139–142. doi: 10.1130/g22921a.1

Naylor, M. (2005). A discrete element model for orogenesis and accretionary wedge growth. *J. Geophys. Res. Solid Earth.* 110, B12403.

Richardson, N. J., Densmore, A. L., Seward, D., Fowler, A., Wipf, M., Ellis, M. A., et al. (2008). Extraordinary denudation in the Sichuan Basin: insights from low-temperature thermochronology adjacent to the eastern margin of the Tibetan Plateau. *J. Geophys. Res.* 113, 55–67.

Royden, L. H., Burchfiel, B. C., and van der Hilst, R. D. (2008). The Geological evolution of the Tibetan Plateau. *Science* 321:1054. doi: 10.1126/science.1155371

Sun, C., Jia, D., Yin, H., Chen, Z., Li, Z., Shen, L., et al. (2016). Sandbox modeling of evolving thrust wedges with different preexisting topographic relief: implications for the Longmen Shan thrust belt, eastern Tibet. *J. Geophys. Res. Solid Earth.* 121, 4591–4614. doi: 10.1002/2016jb013013

Thompson, T. B., Plesch, A., Shaw, J. H., and Meade, B. J. (2015). Rapid slip-deficit rates at the eastern margin of the Tibetan Plateau prior to the 2008 Mw 7.9 Wenchuan earthquake. *Geophys. Res. Lett.* 42, 1677–1684. doi: 10.1002/2014gl062833

Vora, H. B., and Morgan, J. K. (2019). Microscale characterization of fracture growth and associated energy in granite and sandstone analogs: insights using the discrete element method. *J Geophys. Res. Solid Earth* 124, 7993–8012. doi: 10.1029/2019jb018155

Wang, C.-Y., Chen, H.-L., Cheng, X.-G., and Li, K. (2013). Evaluating the role of syn-thrusting sedimentation and interaction with frictional detachment in the structural evolution of the SW Tarim basin, NW China: insights from analogue modeling. *Tectonophysics* 608, 642–652. doi: 10.1016/j.tecto.2013.08.016

Wang, E., and Meng, Q. (2009). Mesozoic and cenozoic tectonic evolution of the Longmenshan fault belt. *Sci. China Ser. D Earth Sci.* 52, 579–592. doi: 10.1007/s11430-009-0053-8

Wang, M., Feng, W., Jiang, D., Yan, B., Chen, Z., and Song, G. (2020). Interactions between thin- and thick-skinned tectonics at the western Sichuan Basin, China. *Tectonophysics* 796:228628. doi: 10.1016/j.tecto.2020.228628

Wang, M., Hubbard, J., Plesch, A., Shaw, J. H., and Wang, L. (2016). Three−dimensional seismic velocity structure in the Sichuan basin, China. *J. Geophys. Res. Solid Earth* 121, 1007–1022. doi: 10.1002/2015jb012644

Wang, X., and Morgan, J. K. (2019). Controls on fore−arc deformation and stress switching after the great 2011 Tohoku−Oki earthquake from discrete numerical simulations. *J. Geophys. Res. Solid Earth* 124, 9265–9279. doi: 10.1029/2019jb017420

Wu, J. E., and McClay, K. R. (2011). Two-dimensional analog modeling of fold and thrust belts: dynamic interactions with syncontractional sedimentation and erosion. *Cardiol. Clin.* 25, 327–334.

Yan, D. P., Qiu, L., Wells, M. L., Zhou, M. F., Meng, X., Lu, S., et al. (2018). Structural and geochronological constraints on the early Mesozoic North Longmen Shan thrust belt: foreland fold-thrust propagation of the SW-Qinling orogenic belt, northeastern Tibetan Plateau. *Tectonics* 37, 4595–4624. doi: 10.1029/2018tc004986

Yang, H., Teng, J.-W., Wang, Q.-S., and Pi, J.-L. (2013). Numerical simulation on the special gravity fields and dynamic response in Longmenshan orogenic belt and adjacent area. *Chin. J. Geophys. Chin. Ed.* 56, 106–116.

Yin, A. (2010). Cenozoic tectonic evolution of Asia: a preliminary synthesis. *Tectonophysics* 488, 293–325. doi: 10.1016/j.tecto.2009.06.002

Yin, A., and Nie, S. (1993). An indentation model for the North and South China collision and the development of the Tan−Lu and Honam fault systems, eastern Asia. *Tectonics* 12, 801–813. doi: 10.1029/93tc00313

Zhang, Y., Jia, D., Shen, L., Yin, H., Chen, Z., Li, H., et al. (2015). Provenance of detrital zircons in the late Triassic Sichuan foreland basin: constraints on the evolution of the Qinling Orogen and Longmen Shan thrust-fold belt in central China. *Int. Geol. Rev.* 57, 1806–1824. doi: 10.1080/00206814.2015.1027967

Zhao, W., Shen, A., Hu, S., Zhang, B., Pan, W., Zhou, J., et al. (2012). Geological conditions and distributional features of large-scale carbonate reservoirs onshore China. *Pet. Explor. Dev.* 39, 1–14. doi: 10.1016/s1876-3804(12)60010-x

Conflict of Interest: ZC and RR were employed by the Research Institute of Petroleum Exploration and Development, Petrochina.

The remaining authors declare that the research was conducted in the absence of any commercial or financial relationships that could be construed as a potential conflict of interest.